

# Systematic Theoretical Analysis of Selective-Mode Plasmonic Filter Based on Aperture-Side-Coupled Slot Cavity

Guangtao Cao · Hongjian Li · Yan Deng · Shiping Zhan ·  
Zhihui He · Boxun Li

Received: 2 January 2014 / Accepted: 28 April 2014 / Published online: 13 May 2014  
© Springer Science+Business Media New York 2014

**Abstract** By taking the aperture as a resonator, we propose an analytical model to describe the dynamic transmission in metal-dielectric-metal (MDM) waveguide aperture-side-coupled with slot cavity. The theoretical results and the finite-difference time-domain (FDTD) simulations agree well with each other, and both demonstrate the mode selectivity and filtering tunability of the plasmonic structure. By adjusting the phase shifts in slot cavity or resonance frequency determined by the aperture, one can realize the required transmission spectra and slow light effect. The theoretical analysis may open up avenues for the control of light in highly integrated optical circuits.

**Keywords** Surface plasmon polariton · Plasmonic filter · Coupled-mode theory · Finite-difference time-domain method · Integrated optics devices

## Introduction

Plasmonic waveguides have shown the considerable potential to transmit and manipulate light below the diffraction limit. Among the wide variety of plasmonic waveguide structures

being investigated, metal-dielectric-metal (MDM) waveguides are of particular interest because they are easily fabricated and have deep subwavelength confinement of light with an acceptable propagation length for surface plasmon polaritons (SPPs) [1–7]. These remarkable advantages have motivated researchers to design and investigate various optical devices in plasmonic MDM waveguide platform, such as splitter [3, 8–11], bend [8, 12, 13], Y-shaped combiner [14], coupler [15, 16], Mach–Zenner interferometer [17], and switch [18–22].

As one of the most prevalent devices in optical circuits, plasmonic filters based on MDM waveguide have been studied widely, including tooth-shaped filter [23–25], multichannel filter [26, 27], channel drop filter with disk resonator [28], rectangular geometry resonator [29, 30], and ring resonator [31]. For the previous studies, 2D MDM-based resonant structures suitable for filtering purposes can be mainly categorized as ring resonator [31, 32], stub [23–25], and cavity [29, 30, 33]. Due to the tight mode confinement in MDM waveguide, resonator excitation via evanescent coupling is both inefficient and challenging to realize even with state-of-the-art electron beam or ion beam lithography. So, aperture coupling was proposed to realize effective coupling [34–37]. However, a systematic theoretical analysis is still lacking for the basic building blocks necessary for the manipulation of SPPs in MDM waveguide aperture-side-coupled with slot cavity.

In this paper, by taking the aperture as a resonator, a more detailed analytical theory for describing the dynamic transmission characteristics in plasmonic filter based on aperture-side-coupled slot cavity is proposed using the temporal coupled-mode theory (CMT) [38]. The consistence between the analytical model and the finite-difference time-domain (FDTD) method validates the feasibility of the theoretical analysis.

G. Cao · H. Li (✉) · S. Zhan · Z. He · B. Li  
College of Physics and Electronics, Central South University,  
410083 Changsha, People's Republic of China  
e-mail: lihj398@126.com

G. Cao · H. Li  
College of Materials Science and Engineering, Central South  
University, 410083 Changsha, China

Y. Deng  
College of Physics, Mechanical and Electrical Engineering, Jishou  
University, 416000 Jishou, China

## Analytical Model

Figure 1a is a schematic illustration of MDM bus waveguide aperture-side-coupled to slot cavity. The insulator and metal in the structure are air and silver, respectively. The permittivity of silver is characterized by Drude model  $\varepsilon(\omega)=1-\omega_p^2/(\omega^2+i\omega\gamma_p)$ , with  $\omega_p=1.38\times 10^{16}$  rad/s and  $\gamma_p=2.73\times 10^{13}$  rad/s. These parameters are obtained by fitting the experimental results [39].  $\omega$  is the angular frequency of incident light. The main structure parameters are the width of bus waveguide, slot cavity and aperture ( $w$ ), lengths of the left and right slot cavities to aperture center ( $L_1$  and  $L_2$ ), and the gap between the bus waveguide and slot cavity ( $g$ ). When the TM polarization light is incident along  $x$ -axis, SPP wave can be formed on metal-insulator interfaces and confined in the waveguide. Here, the dynamic transmission characteristics of the proposed structure can be analyzed by the CMT, as illustrated in Fig. 1b. With the aperture center as a reference plane, the aperture is taken as a resonator.  $S_{+hn}$  and  $S_{-hn}$  ( $h, n=1, 2$ ) stand for incoming and outgoing waves into the resonator. The temporal evolution of energy amplitude  $a$  of the resonator can be described as

$$\frac{da}{dt} = \left( j\omega_0 - \frac{\omega_0}{Q_i} - \frac{\omega_0}{2Q_1} - \frac{\omega_0}{2Q_2} \right) a + S_{+21} e^{j\theta_0} \sqrt{\frac{\omega_0}{2Q_2}} + S_{+11} e^{j\theta_1} \sqrt{\frac{\omega_0}{2Q_1}} + S_{+12} e^{j\theta_2} \sqrt{\frac{\omega_0}{2Q_1}} + S_{+22} e^{j\theta_3} \sqrt{\frac{\omega_0}{2Q_2}}, \quad (1)$$

where  $Q_i$ ,  $Q_1$ , and  $Q_2$  are cavity quality factors related to intrinsic loss, slot cavity coupling loss, and waveguide cou-

pling loss, respectively.  $\omega_0$  is resonant frequency of the resonator.  $\theta_0$  and  $\theta_3$  ( $\theta_1$  and  $\theta_2$ ) represent the phases of coupling coefficients between resonator and bus waveguide (slot cavity).

With the conservation of energy, we get

$$S_{-22} = S_{+21} e^{-j\theta_0} \sqrt{\frac{\omega_0}{2Q_2}} a, \quad (2)$$

$$S_{-11} = S_{+12} e^{-j\theta_1} \sqrt{\frac{\omega_0}{2Q_1}} a, \quad (3)$$

$$S_{-12} = S_{+11} e^{-j\theta_2} \sqrt{\frac{\omega_0}{2Q_1}} a. \quad (4)$$

In the slot cavity, the wave satisfies the following relations:  $S_{+11}=S_{-11}\sigma_1 \exp(-j\varphi_1)$  and  $S_{+12}=S_{-12}\sigma_2 \exp(-j\varphi_2)$  ( $0 < \sigma_1, \sigma_2 < 1$ ).  $\varphi_1=2\omega \text{Re}(n_{\text{eff}})L_1/c+\delta_1$  and  $\varphi_2=2\omega \text{Re}(n_{\text{eff}})L_2/c+\delta_2$  ( $\sigma_1$  and  $\sigma_2$ ) are phase shifts (loss coefficients) of SPPs mode per round trip in left and right slot cavities of the reference plane, respectively.  $\delta_1$  and  $\delta_2$  are the phase shifts of SPPs mode reflected on the two ends of slot cavity.  $\text{Re}(n_{\text{eff}})$  is the real part of effective index for SPPs in slot cavity [5, 18, 40]. With the boundary conditions of  $S_{+22}=0$ , we finally arrive at the transfer function of the system:

$$t = \frac{S_{-22}}{S_{+21}} = \frac{j\left(\frac{\omega}{\omega_0}-1\right) + \frac{1}{Q_i} + \frac{1}{2Q_1} - \frac{1}{2Q_1} \frac{\left[ \frac{e^{j\phi_1}}{\sigma_1} + \frac{e^{j\phi_2}}{\sigma_2} + e^{j(\theta_1-\theta_2)} + e^{j(\theta_2-\theta_1)} \right]}{1 - \frac{e^{j(\phi_1+\phi_2)}}{\sigma_1\sigma_2}}}{j\left(\frac{\omega}{\omega_0}-1\right) + \frac{1}{Q_i} + \frac{1}{2Q_1} + \frac{1}{2Q_2} - \frac{1}{2Q_1} \frac{\left[ \frac{e^{j\phi_1}}{\sigma_1} + \frac{e^{j\phi_2}}{\sigma_2} + e^{j(\theta_1-\theta_2)} + e^{j(\theta_2-\theta_1)} \right]}{1 - \frac{e^{j(\phi_1+\phi_2)}}{\sigma_1\sigma_2}}}. \quad (5)$$

According to Eq. 5, we can systematically analyze the spectra responses in the aperture-side-coupled nanostructure.

## Simulation Results and Discussions

Figure 2a shows the transmission spectra from the same constructive parameters ( $w=100$  nm,  $g=120$  m,  $L=L_1+L_2=$

600 nm), yet with  $L_1=300, 250, 200, 140, 90$ , and 50 nm. The contour profiles of field  $H_z$  at different wavelengths, for  $L_1=200$  nm, are depicted in Fig. 2b–d. For the plasmonic filter, the resonance modes are denoted by  $\text{TM}_m$  ( $m$  is the number of node of the standing waves in the slot cavity). Using the definition of resonance mode, we aim to investigate the evolution of transmission dips versus  $L_1$ . Figure 2b, d shows the  $z$ -component magnetic field distributions of transmission dips at  $\lambda=433$  and 781.2 nm corresponding to  $\text{TM}_4$  and  $\text{TM}_3$  modes,

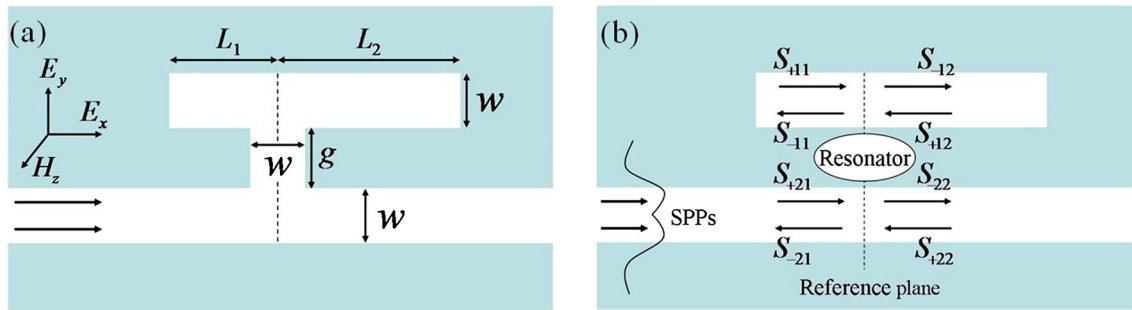


**Fig. 1** **a** Schematic of the plasmonic filter. **b** Equivalent theoretical model for **a**

respectively. Figure 2c depicts the  $z$ -component magnetic field patterns at  $\lambda=553.3$  nm. The results in Fig. 2b–d are in conformity with the transmission spectra in Fig. 2a. In Fig. 2a, the resonant wavelength of TM<sub>4</sub> mode (around 450 nm) oscillates with the variation of  $L_1$ , and the period P<sub>4</sub> is about 170 nm. The full width at half maximum (FWHM) for TM<sub>4</sub> mode is in the range of 11–14 nm, that is to say, it is nearly constant. For the TM<sub>3</sub> mode (around 550 nm), the evolution of resonant wavelength also exhibits periodicity with the change of  $L_1$  from 300 to 50 nm, and the period P<sub>3</sub> is about 210 nm. As  $L_1=300$  or 90 nm, the TM<sub>3</sub> mode is suppressed. The phenomenon for  $L_1=300$  nm has been attributed to the symmetry of plasmonic structure [37]. However, what gives rise to the disappearance of TM<sub>3</sub> mode for  $L_1=90$  nm?

To gain a deep insight into physical mechanism of the phenomena discussed above, we will investigate the transmission spectra versus  $L_1$  and  $\lambda$  by the CMT in the following. For simplicity, we set  $\theta_1=\theta_2$  and  $\sigma_1=\sigma_2$ , then Eq. 5 can be expressed as

$$t = \frac{S_{-22}}{S_{+21}} = \frac{j\left(\frac{\omega}{\omega_0}-1\right) + \frac{1}{Q_i} + \frac{1}{2Q_1} - \frac{1}{2Q_1} \left[ \frac{e^{j\phi_1} + e^{j\phi_2}}{\sigma} + 2 \right]}{j\left(\frac{\omega}{\omega_0}-1\right) + \frac{1}{Q_i} + \frac{1}{2Q_1} + \frac{1}{2Q_2} - \frac{1}{2Q_1} \left[ \frac{e^{j\phi_1} + e^{j\phi_2}}{\sigma} + 2 \right]}. \quad (6)$$

Based on Eq. 6, we discuss the transmission responses  $T=|t|^2$  versus  $L_1$  and  $\lambda$  in Fig. 2e. For the theoretical model,  $\omega_0=4.159 \times 10^{15}$  rad/s,  $Q_i=300$ ,  $Q_1=Q_2=20$ ,  $\sigma=0.98$ ,  $\delta_1=\delta_2=0.6$ , and  $\text{Re}(n_{\text{eff}})=1.26$ . The periodicity of TM<sub>4</sub> and TM<sub>3</sub> modes is well presented. To exhibit the formation and evolution mechanisms of the transmission spectra more explicitly, in Fig. 2f, we show the top view of Fig. 2e. The periods for TM<sub>4</sub> (P<sub>4</sub>) and TM<sub>3</sub> (P<sub>3</sub>) modes are approximately equal to 180 and 210 nm, respectively. The small discrepancy between the FDTD simulations and theoretical results is due to the dispersion of the effective index  $n_{\text{eff}}$  for SPPs. With the variation of  $L_1$ , we only take into account  $\Delta\varphi_1=2\pi\text{Re}(n_{\text{eff}})(L_2-L_1)/\lambda$  (the

variation of  $\varphi_1$ ) for the fixed  $L$ . As  $L_1=90$  nm,  $L=600$  nm,  $\text{Re}(n_{\text{eff}})=1.26$  and  $\lambda=550$  nm, we have  $\Delta\varphi_1=1.9244\pi\approx 2\pi$ . Substituting the above parameters into Eq. 6, we get the identical results to the case of  $L_1=L_2=300$  nm ( $\Delta\varphi_1=0$ ). So, the disappearance of TM<sub>3</sub> mode, for both  $L_1=300$  and 90 nm, arises from  $\Delta\varphi_1=2\pi\text{Re}(n_{\text{eff}})(L_2-L_1)/\lambda=2q\pi$  ( $q$  is an integer) when  $L$  is fixed at 600 nm. By comparing Fig. 2a with Fig. 2f, one can conclude that the theoretical model is consistent with the FDTD method and phase shifts ( $\varphi_1$  and  $\varphi_2$ ) in slot cavity contribute to the periodic variation of transmission dips in the plasmonic structure. Consequently, the theoretical analysis allows us to understand spectral responses of the plasmonic filter system as a function of their microscopic parameters.

Slowing down light in plasmonic structure induces enhanced light-matter interaction and therefore improves the performance of nanoscale plasmonic devices. Group index ( $n_g$ ) in the plasmonic waveguide system can be calculated by the following formula [18, 36]:

$$n_g = \frac{c}{v_g} = \frac{c}{l} \tau_g = \frac{c}{l} \frac{d\theta}{d\omega}, \quad (7)$$

where  $c$  is the speed of light in vacuum,  $\tau_g$  is the optical delay time,  $\theta$  is transmission phase shift,  $v_g$  stands for the group velocity, and  $l$  is the length of the plasmonic system. The dispersion of transmission phase shift versus  $L_1$  and  $\lambda$  is plotted in Fig. 3a, which presents that there is a sudden phase jump around the transmission dip and the phase slope is negative with respect to  $\lambda$ . Figure 3b, c depicts the corresponding optical delay and group index of the plasmonic structure. The maximum optical delay (group index) around TM<sub>4</sub> and TM<sub>3</sub> modes, respectively, are 0.14 ps [35] and 0.12 ps [30]. Furthermore, the group index around TM<sub>4</sub> mode keeps nearly constant versus  $L_1$  but varies periodically around TM<sub>3</sub> mode, which may be promising for the development of ultracompact optical buffers.

In Fig. 4a, we plot a series of transmission spectra versus the relative dielectric constant  $\xi_d$  in slot cavity with the other parameters fixed at  $w=100$  nm,  $g=120$  m, and  $L_1=L_2=300$  nm. Figure 4b shows the wavelength of transmission dips

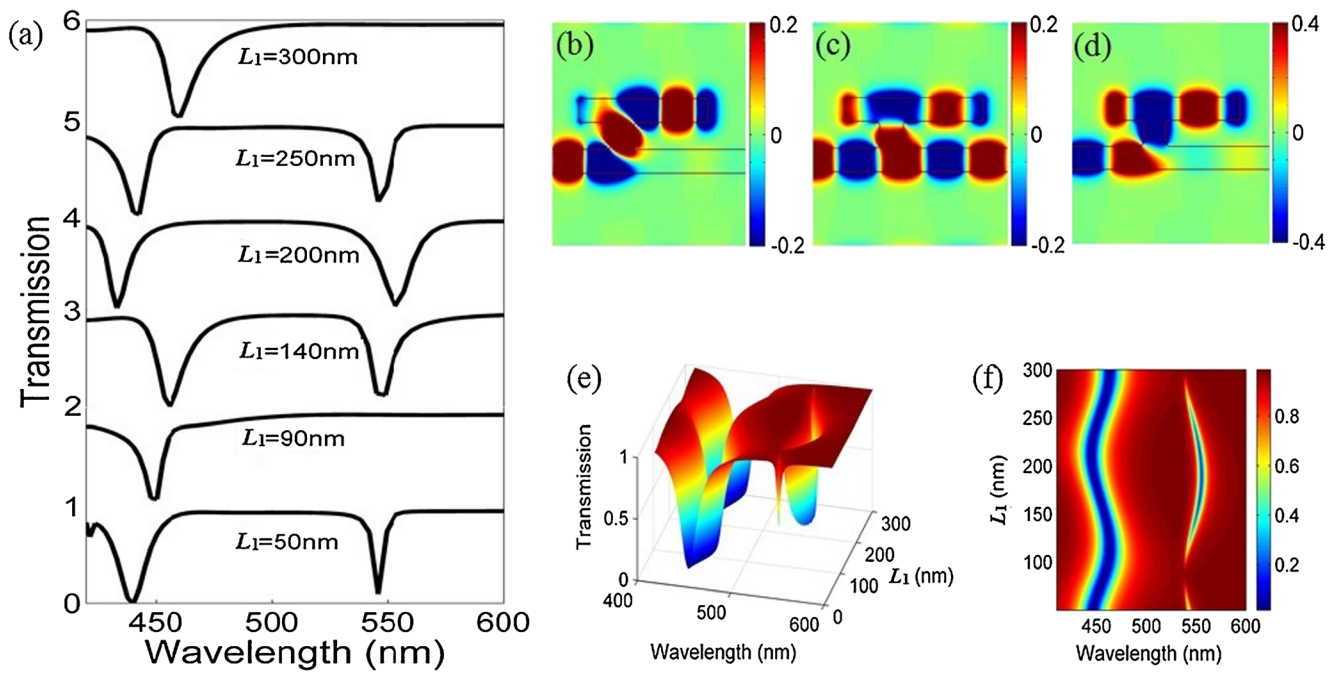


**Fig. 2** **a** Transmission spectra with different  $L_1$ . Field distributions of  $H_z$  in the plasmonic filter at different wavelengths **b**  $\lambda=433$  nm, **c**  $\lambda=553.3$  nm, and **d**  $\lambda=781.2$  nm. The other geometrical parameters are

$w=100$  nm,  $g=120$  nm,  $L_1=200$  nm, and  $L=L_1+L_2=600$  nm. **e** Evolution of the transmission spectra versus  $L_1$  and  $\lambda$ . **f** The top view of **e**

in Fig. 4a with  $\xi_d$  increasing from 1.0 to 1.6. The field distributions  $H_z$  at TM<sub>4N</sub> mode exhibit 4 nodes in the slot cavity, yet with different patterns compared to TM<sub>4</sub> mode (not shown here). It is found that all the wavelengths of resonance modes present red shift and mode spacing increases linearly with the increase of  $\xi_d$ . In this case, due to  $L_1=L_2=L/2$ , Eq. 6 can be rewritten as

$$t = \frac{S_{-22}}{S_{+21}} = \frac{j\left(\frac{\omega}{\omega_0}-1\right) + \frac{1}{Q_i} + \frac{1}{2Q_1} - \frac{1}{Q_1}\frac{1-e^{j\phi}}{1-\frac{\sigma}{\sigma}}}{j\left(\frac{\omega}{\omega_0}-1\right) + \frac{1}{Q_i} + \frac{1}{2Q_1} + \frac{1}{2Q_2} - \frac{1}{Q_1}\frac{1-e^{j\phi}}{1-\frac{\sigma}{\sigma}}} \quad (8)$$

Here, the phase term  $\varphi=\varphi_1=\varphi_2=2\omega\text{Re}(n_{\text{eff}})L_1/c+\delta_1$ . To investigate the transmission spectra in Fig. 4a more explicitly, the real of effective index  $\text{Re}(n_{\text{eff}})$  [5, 18, 40] in the slot cavity ( $w=100$  nm), as a function of relative dielectric constant  $\xi_d$  and incident light wavelength, is illustrated in Fig. 4c. As seen from Fig. 4c,  $\text{Re}(n_{\text{eff}})$  increases apparently with the increase of  $\xi_d$  at a certain wavelength, while  $\text{Re}(n_{\text{eff}})$ , with  $\xi_d$  fixed, varies very slowly in the visible and near infrared. So, adjusting relative dielectric constant  $\xi_d$  is an effective way to manipulate the real of effective index  $\text{Re}(n_{\text{eff}})$  in MDM structure and provides us a method to manipulate phase shifts ( $\varphi_1$  and  $\varphi_2$ ) in slot cavity to control the transmission responses. When the other geometrical and constitutive parameters are fixed,  $\text{Re}(n_{\text{eff}})$  is only related to  $\xi_d$  at a certain wavelength. Based on Eq. 8, the evolution of transmission spectra versus  $\text{Re}(n_{\text{eff}})$

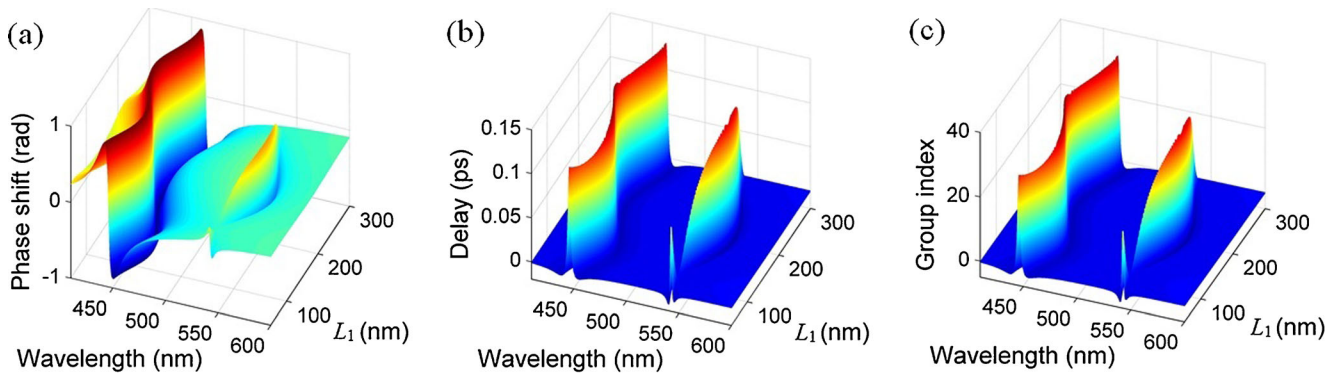


**Fig. 3** Evolution of **a** transmission phase shift, **b** optical delay time, and **c** group index versus  $L_1$  and  $\lambda$

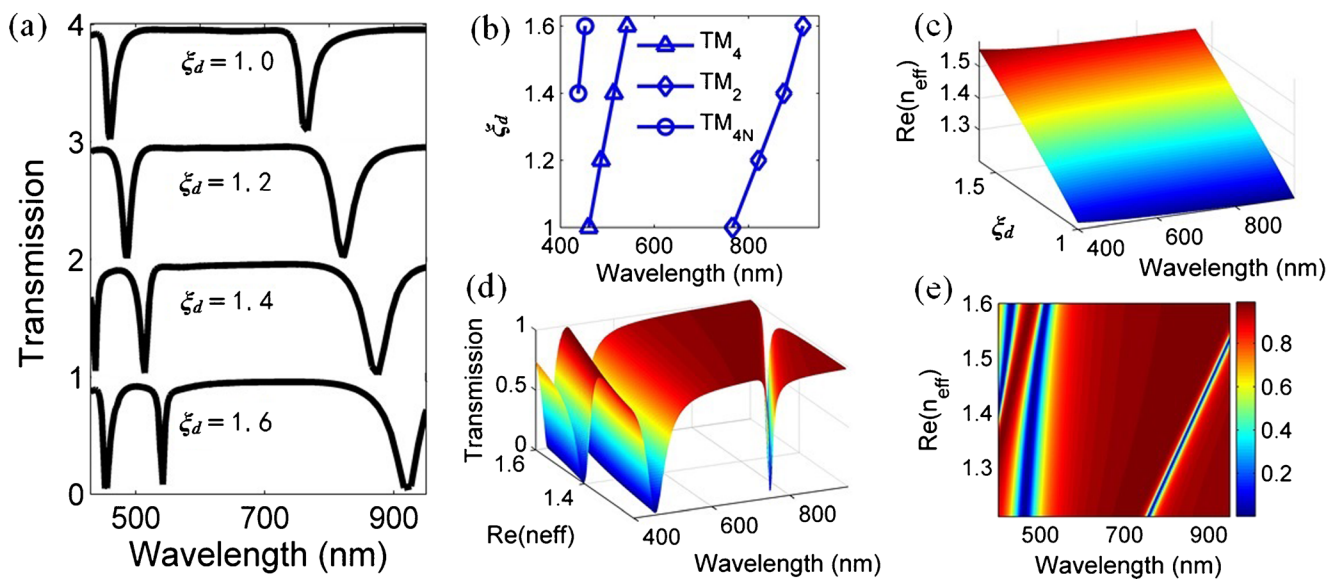


**Fig. 4** **a** Transmission spectra for different relative dielectric constant  $\xi_d$  in the slot cavity. The other geometrical parameters are  $w=100$  nm,  $g=120$  nm, and  $L_1=L_2=300$  nm. **b** The wavelength of the transmission dips in **a** as a function of  $\xi_d$ . **c** Dependence of  $\text{Re}(n_{\text{eff}})$  in slot cavity on the

wavelength of incident light and the relative dielectric constant  $\xi_d$ . **d** Evolution of the transmission spectra versus  $\text{Re}(n_{\text{eff}})$  and  $\lambda$ . **e** The top view of **d**

and  $\lambda$  is plotted in Fig. 4d, of which the top view is shown in Fig. 4e. We can see that the theoretical results are in good agreement with the FDTD simulations except for a little discrepancy of the FWHM of TM<sub>2</sub> mode, which is caused by the dispersion of  $n_{\text{eff}}$  and cavity quality factors ( $Q_i$ ,  $Q_1$ , and  $Q_2$ ). Combing Figs. 2f and 4e, we conclude that one could realize the required transmission spectra by tuning the phase shifts in slot cavity. Furthermore, from the analytical model, we also obtain that the increase of  $L_1$  ( $\xi_d$ ) will increase the

sensitivity of transmission spectra to  $\xi_d$  ( $L_1$ ) in the plasmonic structure with fixed  $L$ .

From Eqs. 6 and 8, it is clear that  $\omega_0$  (resonance frequency of the resonator shown in Fig. 2b) also affects the transmission properties. In Fig. 5a, the transmission spectra versus gap  $g$  are investigated by the FDTD simulations. The blue and red solid lines correspond to, respectively, the symmetric ( $L_1=L_2=300$  nm,  $w=100$  nm) and asymmetric structures ( $L_1=230$  nm,  $L_2=370$  nm, and  $w=100$  nm). For both cases,

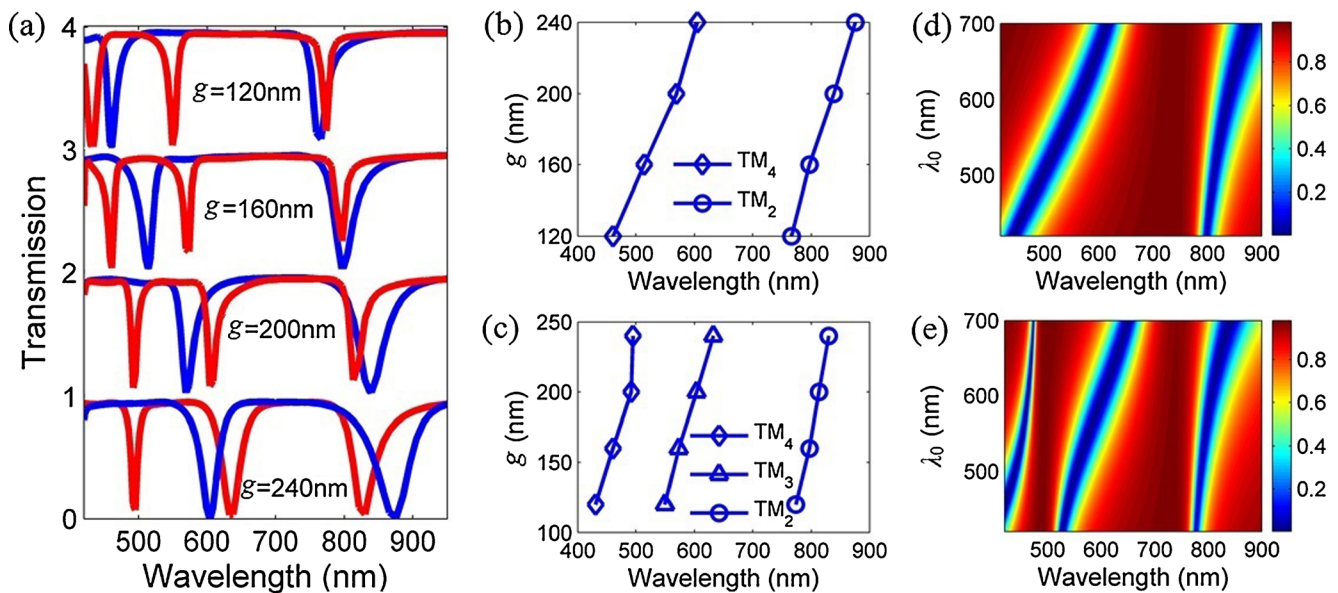


**Fig. 5** **a** Transmission spectra versus different gap  $g$  for symmetric (blue solid line,  $L_1=L_2=300$  nm,  $w=100$  nm) and asymmetric (red solid line,  $L_1=230$  nm,  $L_2=370$  nm, and  $w=100$  nm) structures. The wavelength of transmission dips in **a** as a function of  $g$  for **b** symmetric structure, and **c**

asymmetric structure. Transmission spectra versus  $\lambda_0$  (resonant wavelength of the resonator plotted in Fig. 2b) and incident light wavelength for **d** symmetric and **e** asymmetric structures

Fig. 5b, c shows that the transmission dips exhibit red shift with the increment of  $g$ . The resonance wavelength  $\lambda_0$  (corresponding to  $\omega_0$ ) is determined only by  $g$ , as the other parameters are fixed. So, to investigate the evolution of transmission spectra versus  $g$ , in Fig. 5d, e, we plot the transmission spectra versus resonant wavelength  $\lambda_0$  and incident light wavelength by the analytical model. The transmission spectra in Fig. 5d, e are in good accordance with those in Fig. 5a. For the symmetric case in Fig. 5b, d, the mode spacing between TM<sub>4</sub> and TM<sub>2</sub> modes becomes smaller for larger  $g$ , but TM<sub>3</sub> mode (odd mode) is suppressed, which is attributed to  $\Delta\varphi_1=2\pi\text{Re}(n_{\text{eff}})(L_2-L_1)/\lambda=0$  and similar to the analysis based on the superposition principle of optics and cavity model [33]. For the asymmetric case in Fig. 5c, e, the mode spacing between TM<sub>2</sub> and TM<sub>3</sub> modes decreases with increasing  $g$ , while the mode spacing between TM<sub>3</sub> and TM<sub>4</sub> modes increases. As mentioned above, both the CMT and FDTD methods demonstrate the mode selectivity and filtering tunability of the plasmonic structure with the variation of  $g$ , which further verifies the feasibility of the theoretical analysis.

## Conclusion

In summary, we have derived an analytical model, by taking the aperture as a resonator, for an ultracompact plasmonic filter based on aperture-side-coupled slot cavity. The filter responses obtained theoretically are in good agreement with the rigorous FDTD simulations. Both the theoretical analysis and numerical calculations demonstrate the mode selectivity and filtering tunability of the plasmonic structure. Using the analytical model, we manipulate the transmission properties via phase shifts ( $\varphi_1$  and  $\varphi_2$ ) of SPPs mode in the slot cavity and resonance frequency ( $\omega_0$ ) determined by the aperture, and can also predict the slow light effect. Importantly, the excitation of TM<sub>3</sub> mode (odd mode) for both the symmetric and asymmetric structures depends on whether the relation  $\Delta\varphi_1=2\pi\text{Re}(n_{\text{eff}})(L_2-L_1)/\lambda=2q\pi$  ( $q$  is an integer) is satisfied or not. Moreover, the maximum optical delay (group index) around TM<sub>4</sub> and TM<sub>3</sub> modes are 0.14 ps (35) and 0.12 ps (30), respectively. The results, for the exact and systematic analysis of the selective-mode plasmonic filter, may provide an in-depth understanding of transmission in aperture-side-coupled nanostructure and have potential applications for wavelength-selective, plasmonic sensing, and slow light devices in plasmonic waveguide platforms.

**Acknowledgments** This work was funded by the Fundamental Research Funds for the Central Universities of Central South University under Grant No. 2012zzts007 and 2013zzts009, the Research Fund for the Doctoral Program of Higher Education of China under Grant No.

20100162110068, and the National Natural Science Foundation of China under Grant No. 61275174.

## References

1. Bozhevolnyi SI (2009) Plasmonic nanoguides and circuits. Pan Stanford Publishing Pte. Ltd, Singapore
2. Pile DFP, Ogawa T, Gramotnev DK, Matsuzaki Y, Vernon KC, Yamaguchi K, Okamoto T, Haraguchi M, Fukui M (2005) Two-dimensionally localized modes of a nanoscale gap plasmon waveguide. *Appl Phys Lett* 87:261114
3. Chen JJ, Li Z, Zhang X, Xiao JH, Gong QH (2013) Submicron bidirectional all-optical plasmonic switches. *Sci Rep* 3:1451
4. Park JH, Kim KY, Lee IM, Na HM, Lee SY, Lee BH (2010) Trapping light in plasmonic waveguides. *Opt Express* 18:598–623
5. Economou EN (1969) Surface plasmons in thin films. *Phys Rev* 182: 539–554
6. Gramotnev DK, Bozhevolnyi SI (2010) Plasmonics beyond the diffraction limit. *Nat Photonics* 4:83–91
7. Leveque AG, Szunerits S, Pennec Y, Djafari-Rouhani B, Boukherroub R, Dobrzynski L (2013) Nanometal plasmon polaritons. *Surf Sci Rep* 68:1–67
8. Cai W, Shin W, Fan S, Brongersma ML (2010) Elements for plasmonic nanocircuits with three-dimensional slot waveguides. *Adv Mater* 22:5120–5124
9. Zhang X, Li Z, Chen JJ, Yue S, Gong QH (2013) A dichroic surface-plasmon-polariton splitter based on an asymmetric T-shape nanoslit. *Opt Express* 21:14548–14554
10. Chen JJ, Li Z, Yue S, Xiao JH, Gong QH (2012) Plasmon-induced transparency in asymmetric T-shape single slit. *Nano Lett* 12:2494–2498
11. Chheang V, Lee TK, Oh GY, Kim HS, Lee BH, Kim DG, Choi YW (2013) Compact polarizing beam splitter based on a metal-insulator-metal inserted into multimode interference coupler. *Opt Express* 21: 20880–20887
12. Lee TW, Gray S (2005) Subwavelength light bending by metal slit structures. *Opt Express* 13:9652–9659
13. Guo YN, Wang HN, Reed JM, Pan S, Zou SL (2013) Effective light bending and controlling in a chamber-channel waveguide system. *Opt Lett* 38:2209–2211
14. Gao H, Shi H, Wang C, Du C, Luo X, Deng Q, Lv Y, Lin X, Yao H (2005) Surface plasmon polariton propagation and combination in Y-shaped metallic channels. *Opt Express* 13:10795–10800
15. Veronis G, Fan S (2007) Theoretical investigation of compact couplers between dielectric slab waveguides and two-dimensional metal-dielectric-metal plasmonic waveguides. *Opt Express* 15:1211–1221
16. Rotenberg N, Beggs DM, Sipe JE, Kuipers L (2013) Resonant coupling from a new angle: coherent control through geometry. *Opt Express* 21:16504–16513
17. Wang B, Wang GP (2004) Surface plasmon polariton propagation in nanoscale metal gap waveguides. *Opt Lett* 29:1992–1994
18. Cao GT, Li HJ, Zhan SP, Xu HQ, Liu ZM, He ZH, Wang Y (2013) Formation and evolution mechanisms of plasmon-induced transparency in MDM waveguide with two stub resonators. *Opt Express* 21: 9198–9205
19. Chen L, Gao CM, Xu JM, Zang XF, Cai B, Zhu Y (2013) Observation of electromagnetically induced transparency-like transmission in terahertz asymmetric waveguide-cavities systems. *Opt Lett* 38:1379–1381
20. Piao XJ, Yu S, Park N (2012) Control of Fano asymmetry in plasmon induced transparency and its application to plasmonic waveguide modulator. *Opt Express* 20:18994–18999

21. Lu H, Liu XM, Mao D, Gong YK, Wang GX (2011) Induced transparency in nanoscale plasmonic resonator systems. *Opt Lett* 36:3233–3235
22. Intaraprasong V, Fan SH (2012) Enhancing the waveguide-resonator optical force with an all-optical on-chip analog of electromagnetically induced transparency. *Phys Rev A* 86:063833
23. Lin XS, Huang XG (2008) Tooth-shaped plasmonic waveguide filters with nanometeric sizes. *Opt Lett* 33:2874–2876
24. Tao J, Huang XG, Lin X, Zhang Q, Jin X (2009) A narrow-band subwavelength plasmonic waveguide filter with asymmetrical multiple-teeth-shaped structure. *Opt Express* 17: 13989–13994
25. Pannipitiya A, Rukhlenko ID, Premaratne M, Hattori HT, Agrawal GP (2010) Improved transmission model for metal-dielectric-metal plasmonic waveguides with stub structure. *Opt Express* 18:6191–6204
26. Luo X, Zou XH, Li XF, Zhou Z, Pan W, Yan LS, Wen KH (2013) High-uniformity multichannel plasmonic filter using linearly lengthened insulators in metal–insulator–metal waveguide. *Opt Lett* 38: 1585–1587
27. Wen KH, Yan LS, Pan W, Luo B, Guo Z, Guo YH, Luo XG (2013) Design of plasmonic comb-like filters using loop-based resonators. *Plasmonics* 8:1017–1022
28. Lu H, Liu XM, Mao D, Wang LR, Gong YK (2010) Tunable band-pass plasmonic waveguide filters with nanodisk resonators. *Opt Express* 18:17922–17927
29. Rezaei M, Miri M, Khavasi A, Mehrany K, Rashidian B (2012) An efficient circuit model for the analysis and design of rectangular plasmonic resonators. *Plasmonics* 7:245–252
30. Yun BF, Hu GH, Cui YP (2013) Resonant mode analysis of the nanoscale surface plasmon polariton waveguide filter with rectangle cavity. *Plasmonics* 8:267–275
31. Zand I, Abrishamian MS, Berini P (2013) Highly tunable nanoscale metal-insulator-metal split ring core ring resonators (SRCRRs). *Opt Express* 21:79–86
32. Yu HC, Chen MH, Li PX, Yang SG, Chen HW, Xie SZ (2013) Compact Q-value enhanced bandpass filter based on the EIT-like effect accompanying application in downconversion APL. *Opt Lett* 38:3906–3909
33. Hu F, Yi H, Zhou Z (2011) Band-pass plasmonic slot filter with band selection and spectrally splitting capabilities. *Opt Express* 19:4848–4855
34. Han Z, Van V, Herman WN, Ho PT (2009) Aperture-coupled MIM plasmonic ring resonators with sub-diffraction modal volumes. *Opt Express* 17:12678–12684
35. Nielsen MP, Elezzabi AY (2013) Ultrafast all-optical modulation in a silicon nanoplasmonic resonator. *Opt Express* 21:20274–20279
36. Lu H, Liu XM, Mao D (2012) Plasmonic analog of electromagnetically induced transparency in multi-nanoresonator-coupled waveguide systems. *Phys Rev A* 85:053803
37. Han ZH, Bozhevolnyi SI (2011) Plasmon-induced transparency with detuned ultracompact Fabry-Perot resonators in integrated plasmonic devices. *Opt Express* 19:3251–3257
38. Haus HA (1984) Waves and fields in optoelectronics. Prentice-Hall, Englewood Cliffs, Chapter 7
39. Palik ED (1985) Handbook of optical constants of solids. Academic, Boston
40. Johnson PB, Christy RW (1972) Optical constants of the noble metals. *Phys Rev B* 6:4370–4379